

Article

Optimized Design of Anchor Plates for 2200 MPa-Class Prestressing Anchorage Zones

Xin Lu ^{1,2,3} and Wanxu Zhu ^{1,2,3,*}

¹ College of Mechanical and Control Engineering, Guilin University of Technology, Guilin 541004, China; 2120211168@glut.edu.cn

² Guangxi Key Laboratory of Geotechnical Mechanics and Engineering, Guilin University of Technology, Guilin 541004, China

³ Research Center for Intelligent Structural Materials Engineering, Guilin University of Technology, Guilin 541004, China

* Correspondence: zhuwanxu@vip.163.com

Abstract: The strength of prestressed steel strands has developed towards high strength, increasing from 1860 MPa to over 2200 MPa. The stress in the prestressed anchorage zone is more concentrated and complex, and the anchor plates for dispersed loads need to be optimized in design. This article proposes a design scheme for adding a middle pressure-bearing step based on the existing anchor plate and then establishes a 1/4 model of the concrete anchoring area of the anchor plate for finite element analysis. Based on the theory of the strut-and-tie model, the position of the middle pressure-bearing step is determined according to the maximum angle of the strut-and-tie model. Then, carry out force transfer tests in the anchorage zone for verification. The research results indicate that after adding a middle pressure bearing step to the anchor plate, the angle between the strut-and-tie model in the anchorage zone increases, and the bearing capacity improves. The position of the middle pressure-bearing step in the anchor plate is different, and the angle between the strut-and-tie models is different. According to the middle step position parameter, λ (the ratio of the effective width of the middle step to the distance from the middle step to the end face of the anchor plate) is 0.533 to optimize the anchor plate, and the bearing capacity of its anchorage zone is relatively high. The main tensile and main compressive stresses of the anchor plate after optimization increased by 6.2% and 5.74%, respectively, compared to the anchor plate before optimization. The main tensile stress of the spiral reinforcement under the anchor plate decreased by 0.59%, the main compressive stress decreased by 2.89%, and the von-Mises stress decreased by 2.32%. The side surface tensile stress of concrete under the anchor plate was reduced by 4.3 percent. Finally, three concrete specimens were poured for force transfer testing in the anchorage zone, verifying the safety and reliability of the optimized anchor plate in the 2200 MPa-level prestressed anchorage zone.

Keywords: 2200 MPa prestressed; anchorage zone; the strut-and-tie model; anchor plate



Citation: Lu, X.; Zhu, W. Optimized Design of Anchor Plates for 2200 MPa-Class Prestressing Anchorage Zones. *Buildings* **2024**, *14*, 1073. <https://doi.org/10.3390/buildings14041073>

Academic Editor: Alberto Taliervo

Received: 15 March 2024

Revised: 31 March 2024

Accepted: 10 April 2024

Published: 12 April 2024



Copyright: © 2024 by the authors. Licensee MDPI, Basel, Switzerland. This article is an open access article distributed under the terms and conditions of the Creative Commons Attribution (CC BY) license (<https://creativecommons.org/licenses/by/4.0/>).

1. Introduction

For prestressing the strand in the direction of high-strength development, the higher its strength, the more significant the economic benefits. At present, 2200 MPa-level strands can be mass-produced, but the performance of the anchor plate supporting the prestressing anchorage system is doubtful. In particular, the strand strength increase leads to its prestressing anchorage zone being more concentrated and complex, and the anchor plate may have insufficient bearing capacity and cracking. Therefore, the optimal design of the anchor plate to meet the high-strength strand is very important and urgent.

Many scholars at home and abroad have done a lot of experimental studies and finite element analyses on the design of anchor plates. Overseas, Reblo J [1] and Shin J [2] studied the concrete force transfer performance in the anchorage zone of the anchor plate and found that the thickness of the anchor plate had a greater effect on the local

compressive load-bearing capacity. Yangsu Kwon [3] established an anchorage zone model for finite element analysis through load transfer experiments on 18 locally pressurized specimens and studied the effects of the position, number, and length of the ribs of the anchor plate on the load-bearing capacity of the anchorage zone. Jianghao Ji [4] established a three-dimensional model of the anchorage zone using a secondary pressure-bearing step anchor plate and carried out finite element analysis and load transfer tests using ABAQUS. Cervenka [5] carried out finite element analysis of the anchorage zone using a GC-type anchor plate using the cross-section shape of the anchorage zone as a variable, respectively, and concluded that a rectangular cross-section of the anchor zone resulted in a reduction of the load-bearing capacity, and the square cross-section has good load-carrying capacity. Mao W [6] investigated 1860 MPa grade prestressing anchorage zones using YM15-31 as well as YM15-19 anchorage zones, respectively, and concluded that YM15-31 anchorage zones exhibited good mechanical properties and elastic conditions under eight different loads. Jin Kook Kim [7] took the presence or absence of transverse ribs in the anchor plate as a variable to establish its three-dimensional anchorage zone. The finite element analysis and load transfer experiments were carried out, and it was concluded that the addition of transverse ribs to the internal structure of the anchor plate can greatly disperse the concentrated stresses in the anchorage zone and improve the local bearing capacity of the concrete anchorage zone. In China, Chen Daosen [8] developed a new environmentally friendly 1860 MPa grade prestressing anchorage zone anchor plate; the Marin team [9] designed a high-strength 2000 MPa grade prestressing anchorage zone anchor plate. Ma Qian [10] designed an 1860 MPa-grade compact stepped anchor plate for prestressing anchorage zones. Zhao Yong [11] studied the prestressed concrete anchorage zone force transfer performance of domestically cast mat plates by completing the load transfer test of 38 localized pressure-bearing specimens and concluded that the ultimate load-carrying capacity of the anchorage zone could be improved by setting the secondary flange on the flared pipe as well as enlarging the pressure-bearing area of the anchorage zone. Chen Jiayi [12] took the Hangzhou Bending Sea Bridge as an example to establish a 1/2 model for finite element analysis of prestressed concrete box girder under two different anchor plates, and based on the comparison of experimental and theoretical analyses, it was concluded that the anchor plates and the end circular ribs were jointly involved in the prestressing force transfer and that the maximum tensile stresses and compressive stresses occurred locally on the lower side of the anchor plates. Zhu Wanxu team [13,14] in the Hong Kong-Zhuhai-Macao Bridge segmental prefabricated abutment high-strength rebar joint anchorage system development, through the finite element analysis and load transfer test, to verify the reasonableness of the design of the anchor plate of the secondary compression structure. The increase of the anchor plate of the secondary compression structure effectively improves the anchorage zone of the compression zone, ensures the reliability of the high-strength threaded rebar anchorage, and will be the success of this technology used in the construction of the Hong Kong-Zhuhai-Macao Bridge. However, under the condition of not changing the strength of the strand, the original external dimensions of the anchor plate are maintained, and the design of the anchor plate is optimized for the promotion of the anchor plate. Based on the anchor plate of the two-stage compression structure, the intermediate third-stage compression structure step is added to increase the contact area between the anchor plate and the concrete, improve the force transmission performance between the anchor plate and the concrete, and reduce the stress concentration. It is doubtful whether the concrete bearing capacity under the anchor is sufficient. Therefore, it is necessary to carry out further research on this.

In summary, there is little literature on the structural design of anchor plates in 2200 MPa-class prestressing anchorage zones. This paper proposes a method to optimize the design of the internal structure of the anchor plate based on the theory of the strut-and-tie model, to increase the position of the intermediate pressure-bearing step as a variable, to explore the change of the clamping angle of the strut-and-tie model in the anchorage zone,

and to determine the optimal position of the intermediate pressure-sharing step according to the maximum clamping angle of the strut-and-tie model. The safety and reliability of the anchor plate after optimization are verified by finite element comparative analysis and force transmission test in the anchorage zone.

2. Theoretical Analysis

2.1. Basic Configuration of the Strut-and-Tie Model

The strut-and-tie model developed from truss structures as a new approach to solving the D-zone of concrete structures. Structural D-zone mainly exists in stress concentration, and the anchorage zone is suitable for simplified characterization by the strut-and-tie model because the stress concentration in the anchorage zone is more complex due to the development of the strength of prestressing strands to a higher level [15–20]. Due to the localized pressure effect, the localized pressure is too high, and two types of failures occur in the strut-and-tie model. The failure of the compression bar leads to damage to the anchorage zone, which is manifested as cracks on the concrete surface [21–25]. The failure of the tie rod is manifested as cracking on the side surface of the concrete spreading the damage. To improve the bearing capacity of the anchorage zone, as shown in Figure 1, the solid line is the anchor plate before optimization, and the dotted line is the anchor plate after optimization. α is the angle of the anchor plate before optimization, and β is the angle of the anchor plate after optimization.

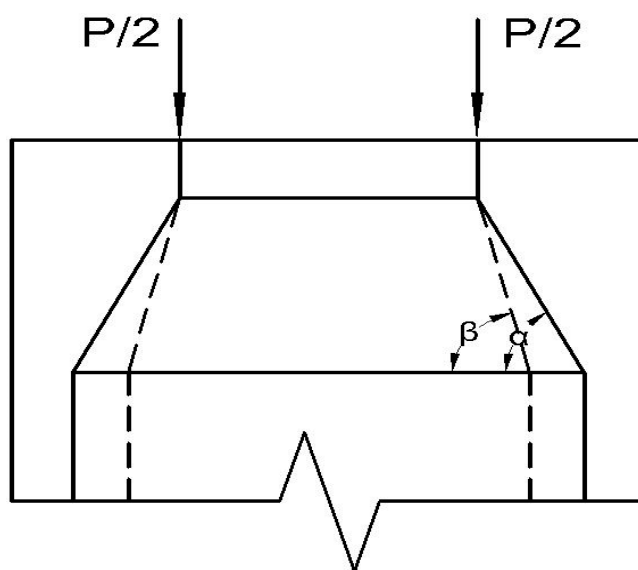


Figure 1. The strut-and-tie model in the anchorage zone.

The expression of bearing capacity and the internal force of the tension rod in the strut-and-tie model is as follows:

$$F_a = \tan \theta F_c \quad (1)$$

In the formula, F_a is the prestressing force; θ is the angle between the pull rod and the compression rod of the strut-and-tie model; F_c is the internal force of the tension rod. From Equation (1), it can be seen that the bearing capacity is improved by increasing the angle of the strut-and-tie model. From Figure 1, it can be seen that at the dashed line after optimization of the strut-and-tie model, the length of the pull rod depends on the internal force of the pull rod. The length of the pull rod becomes shorter, and the position of the pull rod remains unchanged. The angle between the tension rod and the compression rod in the strut-and-tie model increases, resulting in an increased bearing capacity.

2.2. Angle Calculation of the Strut-and-Tie Model

According to the theory of the anchorage zone strut-and-tie model, it can be seen that in the strut-and-tie model, the tensile bar generally consists of steel reinforcement, prestressing tendons, or concrete tensile zone, so the internal force of the tensile bar can be expressed as follows:

$$T_b = \frac{\sum_{n=1}^m T_n d_n}{d} \quad (2)$$

where: T_b is the internal force of the tie rod; T_n is the tension of the n steel bar or the n tension in the tension zone; d_n is the distance from the n steel bar or the n tension in the tension zone to the top surface; d is the distance between the tie rod and the top surface.

$$\theta = \arctan \frac{p}{2T_b} \quad (3)$$

where: θ is the angle between the pull rod and the compression rod of the strut-and-tie model; p is for prestress.

Substitute the Formula (2) into (3) to get the following:

$$\theta = \arctan \frac{pd}{2 \sum_{n=1}^m T_n d_n} \quad (4)$$

3. The Anchoring Zone Model Was Established

According to the requirements of the specification [26], the external dimensions of the anchor plate are shown in Figure 2. The UG three-dimensional modeling software was used to establish a three-dimensional model of the 2200 MPa-class prestressing anchorage zone imported into the finite element modeling software ANSYS 2022R1 version for finite element analysis, and the three-dimensional model is shown in Figure 3.

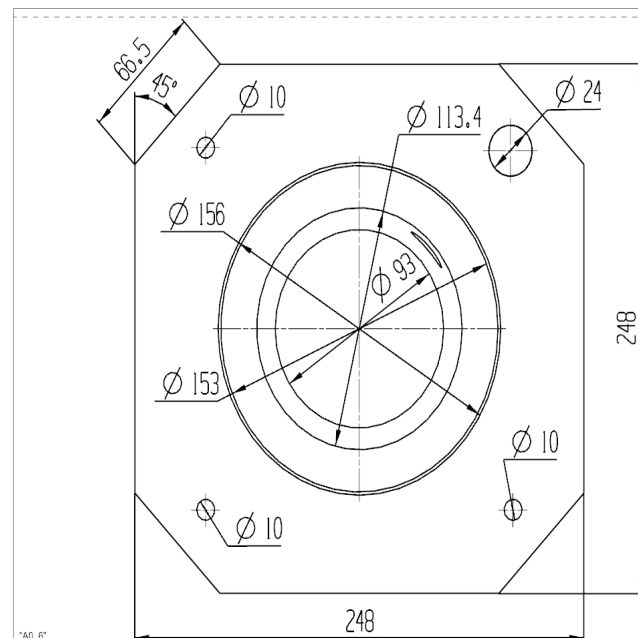


Figure 2. Anchor plate external dimensions.

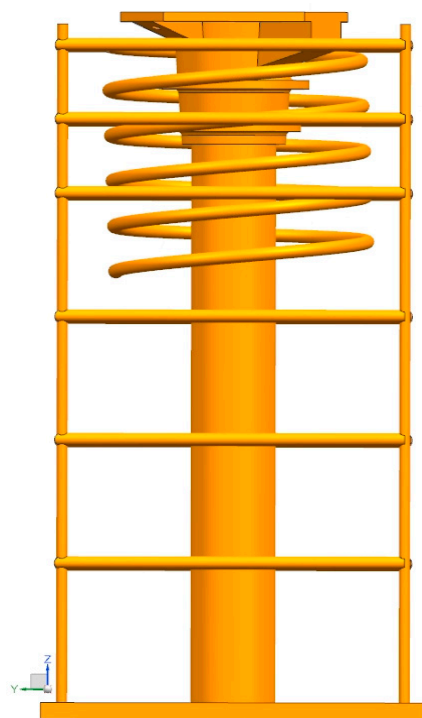


Figure 3. Schematic diagram of finite element analysis model.

4. Finite Element Analysis

4.1. Finite Element Analysis of Model

Model Overview

The anchor plate is an ideal elastic-plastic material; Solid186 solid cells are selected; 8-node Solid65 solid cells are used for concrete; and Pipe16 rod cells are used for spiral reinforcement. The meshing is done by hexahedral meshing. In the simulation analysis, the anchor plate before the optimization is the anchor plate with a second-order pressure-bearing step, and the anchor plate after optimization is the anchor plate with an increased intermediate pressure-bearing step. Without affecting the overall stress of the model, the grouting holes are ignored, and the 1/4 model is selected for finite element analysis according to the symmetry of the structure. The material parameters are shown in Table 1.

Table 1. Material parameters.

Material Name	Poisson's Ratio	Young's Modulus/GPa	Tensile Strength/MPa	Compressive Strength/MPa
Concrete of C50	0.2	34.5	1.89	33.5
Anchor plate of HT200	0.3	135	200	200
Reinforcement frame of HRB400	0.3	210	360	360
Spiral reinforcement of HPB300	0.3	210	270	270

According to the actual load transfer test mode, a uniform load is applied to the bearing surface where the anchor plate is located, and the load value is $F = \frac{1}{4} \times 0.75 \times 9 \times 2200 \times 140 \times 10^{-3} = 519.75$ kN; The bottom surface of the model is supported and constrained by the symmetric surface.

4.2. The Strut-and-Tie Model Analysis

According to related scholars, Zhao established [27] that arranging the tie rods near the location of the expansion cracking stress can effectively restrain the expansion cracking force. In this paper, the stress trace method is used to generate the main tensile and

compressive stress traces through finite element analysis (see Figures 4 and 5) and establish the strut-and-tie model (see Figure 6).

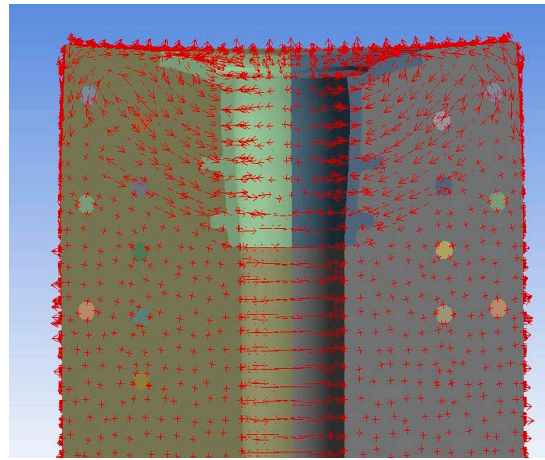


Figure 4. Principal tensile stress trace in the anchoring zone.

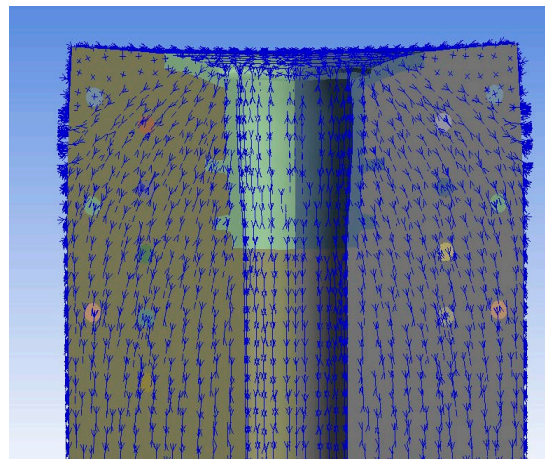


Figure 5. Principal compressive stress trace in the anchoring zone.

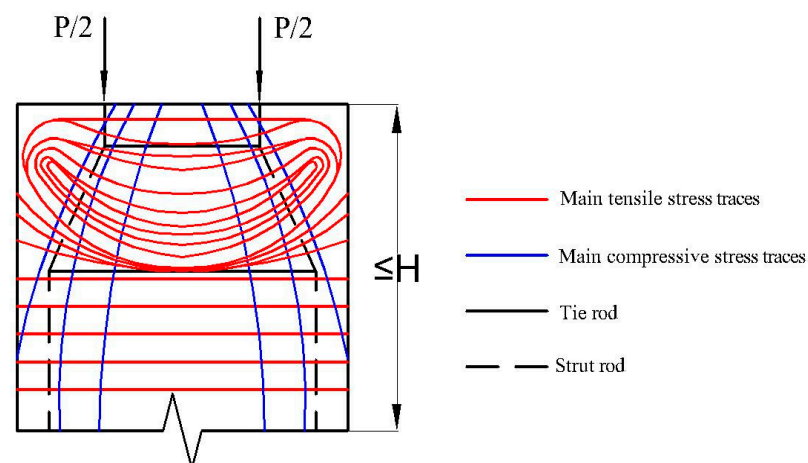


Figure 6. Establishing the strut-and-tie model.

To investigate the different positions of the middle bearing step of the anchor plate before optimization and the change of the angle between the tie rod and the compression rod of the strut-and-tie model, the positional parameter λ of the middle bearing step of the anchor plate was introduced (the ratio of the distance from the effective width of the middle

step of the anchor plate to the end face of the anchor plate to the effective width of the middle bearing step of the anchor plate), and the middle bearing step was gradually shifted downward from the axial stiffener rib close to the grouting holes in 5 mm increments, and a comparative analysis of nine sets of anchorage zones in different positions of the anchor plate with different locations of the middle bearing step was carried out, compared to the finite element analysis of the anchorage zone of the preoptimization anchor plate. The addition of anchor plates corresponding to the different positional parameters of the intermediate pressure-bearing steps is shown in Figure 7.

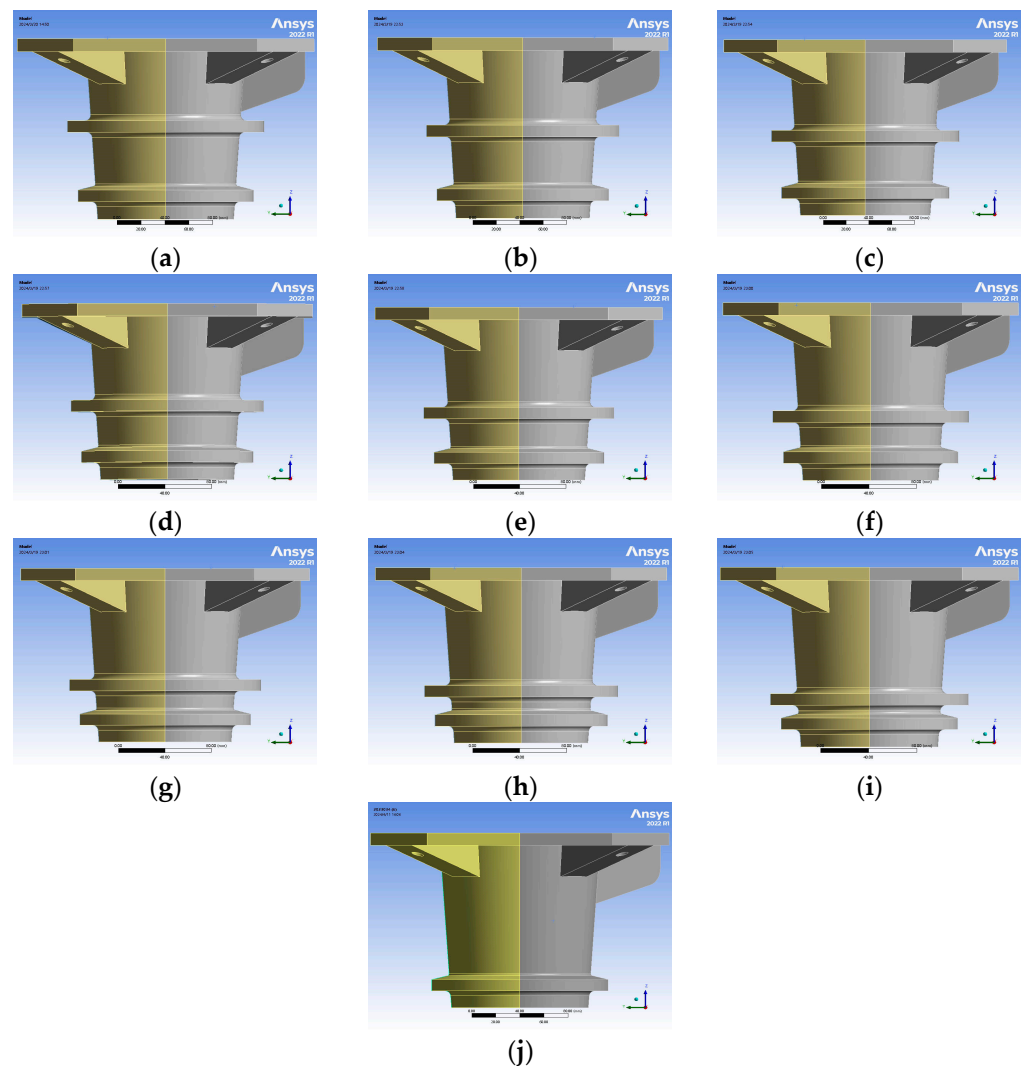


Figure 7. Anchor plates corresponding to different positional parameters. (a) $\lambda = 0.473$. (b) $\lambda = 0.503$. (c) $\lambda = 0.533$. (d) $\lambda = 0.564$. (e) $\lambda = 0.594$. (f) $\lambda = 0.625$. (g) $\lambda = 0.655$. (h) $\lambda = 0.686$. (i) $\lambda = 0.716$. (j) $\lambda = 0$.

The results of the analysis yielded the relationship between the positional parameters of the intermediate pressure-bearing step and the angle of the strut-and-tie model, as shown in Table 2.

As can be seen from Figure 8, adding intermediate pressure-bearing steps based on the anchor plate of the secondary pressure-sharing structure increases the angle of the strut-and-tie model of the anchorage zone, and the bearing capacity of the anchorage zone is increased. The anchorage zone strut-and-tie model angle varies depending on the location of the anchor plate with the addition of the intermediate pressure-bearing step. The anchor plate with an increased intermediate bearing step location parameter of 0.533 has the largest angle of the anchorage zone strut-and-tie model. Therefore, the anchor plate optimized according to the intermediate pressure-bearing step position parameter 0.533 (see Figure 9)

has a relatively high bearing capacity in the anchorage zone. Before the optimization of the anchor plate, the internal force of the strut-and-tie model in the anchorage zone was calculated to be 132.67 kN, and the angle between the strut-and-tie was 62.96° according to the finite element analysis. After the optimization of the anchor plate, the internal force of the strut-and-tie model in the anchorage zone is calculated to be 131.04 kN, and the angle between the strut-and-tie is 63.24° according to the finite element analysis.

Table 2. Comparison of tie rod internal force in anchorage zone with angle of strut-and-tie model for Anchor plate with different positional parameters.

Position Parameter	Internal Force on the Tie Rod/kN	Strut-and-Tie Model Clamp Angle/ $^\circ$
0	132.67	62.96
0.473	131.26	63.20
0.503	131.16	63.21
0.533	131.04	63.24
0.564	131.73	63.12
0.594	131.53	63.15
0.625	131.41	63.17
0.655	131.46	63.16
0.686	131.22	63.21
0.716	131.36	63.18

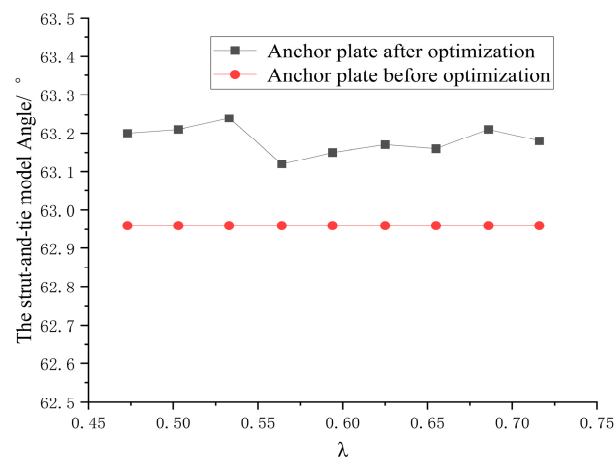


Figure 8. Relation between the position parameters of the middle-pressure step and the angle of the strut-and-tie model.

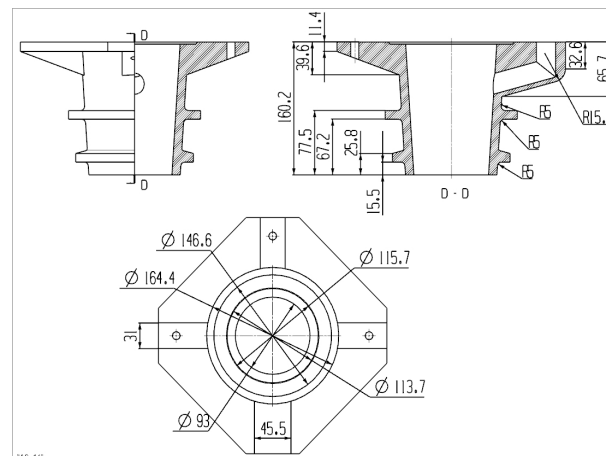


Figure 9. Optimized internal construction dimensions of the anchor plate.

4.3. Comparison of Finite Element Calculation Results

From Figure 10, it can be seen that the main tensile stress of the anchor plate with intermediate pressure-bearing step position parameter 0.533 is 70.91 MPa, which is 7% larger than the average value of the main tensile stress of the anchor plate with other intermediate pressure-bearing step position parameters, and the main tensile stress of the anchor plate before the optimization is 6.2% larger than that before optimization. The main tensile stresses in the anchor plates with parameters of 0.533, 0.564, 0.594, 0.655, and 0.686 for the location of the intermediate pressure-bearing steps are larger by 2.99% to 6.63% than those of the anchor plates before optimization. From Figure 11, it can be seen that the main compressive stress of the anchor plate with an intermediate bearing step position parameter of 0.533 is the largest, with a value of 147.32 MPa, which is 7.38% larger than the average value of the main compressive stress of the anchor plate with the other increase in the intermediate bearing step position parameter, and the main compressive stress of the anchor plate before the optimization is increased by 5.74%. The anchor plate's main compressive stresses for the intermediate bearing step location parameters of 0.473 and 0.533 are 2.44% to 5.74% greater than the anchor plate before optimization. The maximum main tensile stress and main compressive stress of the anchor plate did not exceed its material tensile or compressive strength limit of 200 MPa, which meets the specification limits [26]. The comparative finite element analysis of the anchor plate before and after the optimized design is shown in Table 3. In the table, A_1 is used to indicate the main tensile stress of the anchor plate after optimization, A_0 is used to indicate the main tensile stress of the anchor plate before optimization, B_1 is used to indicate the main compressive stress of the anchor plate after optimization, and B_0 is used to indicate the main compressive stress of the anchor plate before optimization.

As can be seen from Figure 12, the main tensile stress of the spiral reinforcement under the anchor plate with the position parameter of 0.533 intermediate pressure step is 0.16% to 4.37% larger than that under the anchor plate with the increased intermediate pressure step. The main tensile stress of the spiral reinforcement under the anchor plate with the location parameter of the intermediate bearing step of 0.533 is 36.82 MPa, which is 1.49% larger than the average value of the main tensile stress of the spiral reinforcement under the anchor plate with the location parameter of the intermediate bearing step, and the tensile stress of the spiral reinforcement under the anchor plate before the optimization is reduced by 0.59%. The main tensile stress of the spiral reinforcement under the anchor plate before optimization is 0.16–4.37% greater than that under the anchor plate after optimization. As can be seen in Figure 13, the main compressive stress of the spiral reinforcement under the anchor plate with the intermediate pressure-bearing step position parameter of 0.533 is 9.27 MPa, which is 3.13% smaller than the average value of the main compressive stress of the spiral reinforcement under the anchor plate at the other intermediate pressure-bearing step position parameter, and it increases by 2.89% compared with that of the main compressive stress under the anchor plate before the optimization. The main compressive stresses in the spiral reinforcement under the anchor plate with intermediate bearing step location parameters of 0.473, 0.503, 0.533, 0.564, 0.594, 0.625, 0.655, and 0.716 were 2~14.76% greater than the main compressive stresses in the spiral reinforcement under the anchor plate before optimization. Before and after the optimization design of the anchor plate, the comparative finite element analysis of the spiral reinforcement under the anchor plate is shown in Table 4. In the table, C_1 indicates the main tensile stress of the spiral reinforcement under the anchor plate after the optimization of the anchor plate, C_0 indicates the main tensile stress of the spiral reinforcement under the anchor plate before the optimization of the anchor plate, D_1 indicates the main compressive stress of the spiral reinforcement under the anchor plate after the optimization of the anchor plate, and D_0 indicates the main compressive stress of the spiral reinforcement under the anchor plate before the optimization of the anchor plate.

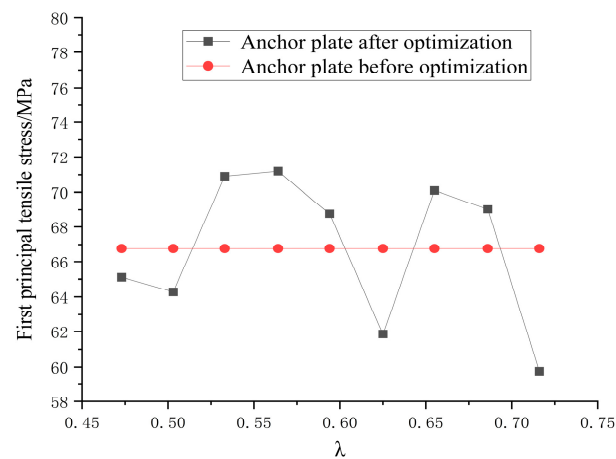


Figure 10. Comparison of the first principal tensile stress in the anchor plate.

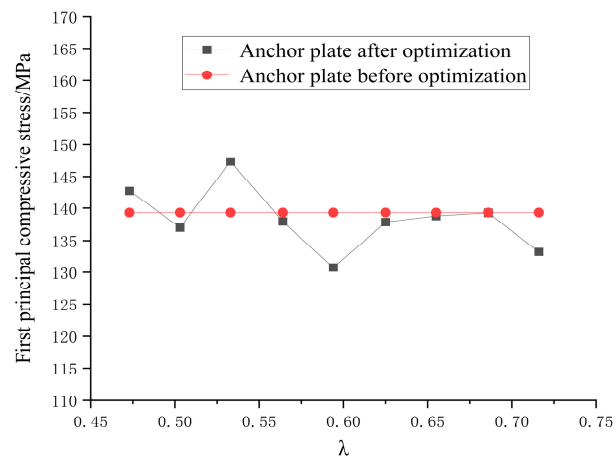


Figure 11. Comparison of the first principal compressive stress in the anchor plate.

Table 3. Comparative finite element analysis of anchor plate after optimization and anchor plate before optimization.

Position Parameter (λ)	A_1 /MPa	A_0 /MPa	B_1 /MPa	B_0 /MPa
0.473	65.11	66.77	142.72	139.32
0.503	64.26	66.77	137.01	139.32
0.533	70.91	66.77	147.32	139.32
0.564	71.20	66.77	137.96	139.32
0.594	68.77	66.77	130.75	139.32
0.625	61.86	66.77	137.86	139.32
0.655	70.11	66.77	138.80	139.32
0.686	69.03	66.77	139.28	139.32
0.716	59.77	66.77	133.25	139.32

As can be seen from Figure 14, the von-mises tensile stress of the spiral reinforcement under the anchor plate with a position parameter of 0.533 in the middle bearing step is 63.49 MPa, which is 2.02% smaller than the average value of the von-mises tensile stress of the spiral reinforcement under the anchor plate with other position parameters and 2.32% smaller than that of the von-mises tensile stress of the spiral reinforcement under the anchor plate before optimization. The von-mises tensile stresses of the spiral reinforcement under the anchor plate with intermediate bearing step location parameters of 0.564, 0.655, and 0.716 are 2~3.22% greater than the von-mises tensile stresses of the spiral reinforcement under the anchor plate before optimization. As can be seen from

Figure 15, adding the intermediate third pressure-bearing step on top of the anchor plate with the second pressure-bearing step reduces the tensile stress on the concrete side surface of the anchorage zone and increases the bearing capacity. The side surface tensile stress on the concrete in the anchorage zone of the anchor plate before the optimization is 1.53~4.49% greater than that of the anchor plate with the addition of an intermediate pressure-bearing step. The anchor plate with the 0.533 intermediate bearing step position parameter has the smallest concrete side surface tensile stress in the anchorage zone, with a value of 4.45 MPa, which is 1.33% smaller than the average value of the concrete side surface tensile stress in the anchorage zone of the anchor plate with the other intermediate bearing step position parameter and 4.3% smaller than that of the anchor plate before optimization. The maximum value of tensile stress on the concrete surface does not exceed 5 MPa (1/10 of the concrete compressive strength) when the model is in the linear elastic phase. Therefore, the anchor plate is optimally designed with an intermediate pressure-bearing step location parameter of 0.533, which has a relatively high bearing capacity in the anchorage zone. Before and after anchor plate optimization, the comparative finite element numerical simulation analyses of the stresses in the lower spiral reinforcement of the anchor plate and the tensile stresses on the side surface of the concrete are shown in Table 5. In the table, E_1 is used to denote the von-mises tensile stress of the spiral reinforcement under the anchor plate after optimization, E_0 is used to denote the von-mises tensile stress of the spiral reinforcement under the anchor plate before optimization, F_1 is used to denote the tensile stress on the side surface of the concrete under the anchor plate after optimization, and F_0 is used to denote the tensile stress on the side surface of the concrete under the anchor plate before optimization.

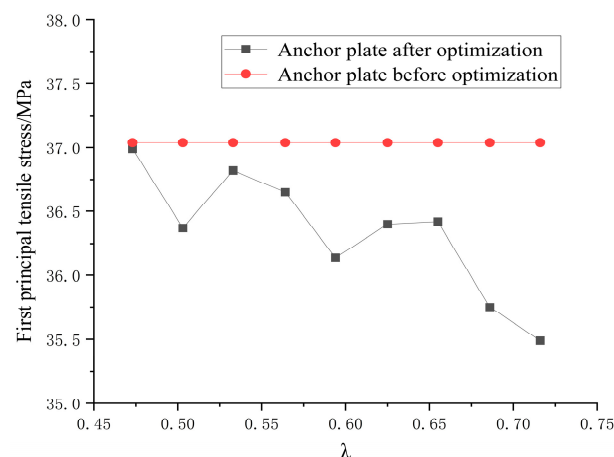


Figure 12. Comparison of the first principal tensile stress of the spiral reinforcement.

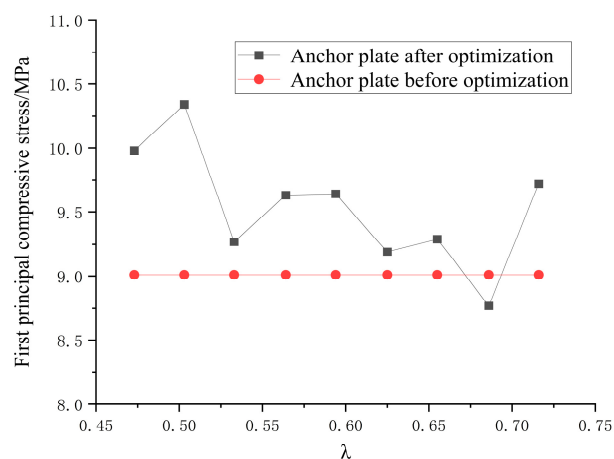
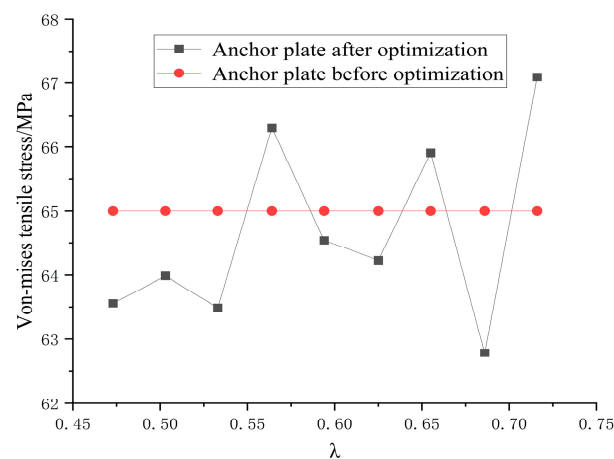
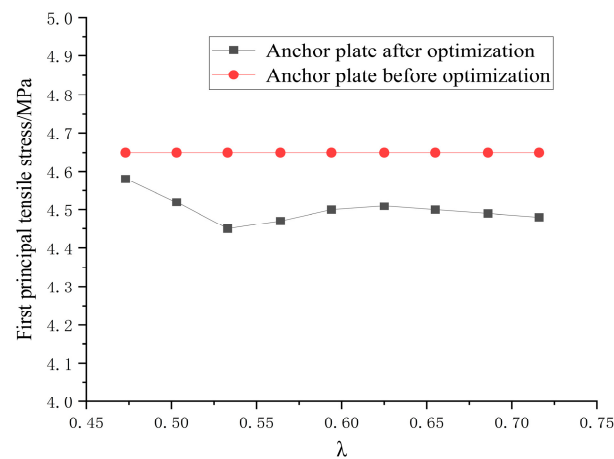


Figure 13. Comparison of the first principal compressive stress of the spiral reinforcement.

Table 4. Comparative finite element analysis of spiral reinforcement under its anchor plate before and after anchor plate optimization.

Position Parameter (λ)	C_1 /MPa	C_0 /MPa	D_1 /MPa	D_0 /MPa
0.473	36.99	37.04	9.98	9.01
0.503	36.37	37.04	10.34	9.01
0.533	36.82	37.04	9.27	9.01
0.564	36.65	37.04	9.63	9.01
0.594	36.14	37.04	9.64	9.01
0.625	36.40	37.04	9.19	9.01
0.655	36.42	37.04	9.29	9.01
0.686	35.75	37.04	8.77	9.01
0.716	35.49	37.04	9.72	9.01

**Figure 14.** Comparison of von-mises tensile stresses in spiral reinforcement.**Figure 15.** Comparison of the first principal tensile stress on the side surface of the concrete.**Table 5.** Comparative analysis of spiral reinforcement von-mises stresses as well as concrete side surface tensile stresses before and after anchor plate optimization.

Position Parameter (λ)	E_1 /MPa	E_0 /MPa	F_1 /MPa	F_0 /MPa
0.473	63.56	65.00	4.58	4.65
0.503	63.99	65.00	4.52	4.65
0.533	63.49	65.00	4.45	4.65
0.564	66.30	65.00	4.47	4.65
0.594	64.54	65.00	4.50	4.65
0.625	64.23	65.00	4.51	4.65
0.655	65.91	65.00	4.50	4.65
0.686	62.78	65.00	4.49	4.65
0.716	67.09	65.00	4.48	4.65

5. Load Transfer Test

5.1. Test Method

The loading method selected for the anchorage zone force transfer test is monotonic load holding loading, and the loading test machine directly applies compressive stress to the anchor plate to simulate the tensioning process of the prestressing strand. Casting anchor plate processing technology: first, prepare the casting model through the shell and core body machine using coated sand to manufacture the shell and core body, and then the drying sand core is placed to close the box to complete the anchor plate casting model production. Secondly, smelt the steel. Further, a deoxidizer is added to the molten steel to deoxidize it. Finally, the refined steel will be cast into the casting model to form the preliminary shape of the anchor plate. The physical drawing of the anchor plate is shown in Figure 16. The test needs a YES-500 hydraulic pressure test instrument, a working anchor plate, three concrete cube test blocks, a fiber grating strain sensor, a CW60 crack width tester, two spectral demodulation instruments, and a computer. The test equipment and test blocks are shown in Figure 17.



Figure 16. Physical picture of the anchor plate.



Figure 17. Test equipment and test block.

The concrete specimens were placed on the loading bench, the working anchor plate was placed on the end face of the inner ring countersink of the anchor plate, and the working anchor plate was loaded by the loading tester. Firstly, 10% F_{ptk} (F_{ptk} is the design load of the anchor plate) was applied for pre-pressure to ensure that each fiber-optic grating strain transducer began to work normally after applying pressure, and then reloaded step by step in increments of 20% F_{ptk} , and then loaded at 20% F_{ptk} , 40% F_{ptk} , 60% F_{ptk} , 80% F_{ptk} , 100% F_{ptk} , 120% F_{ptk} , respectively, hold the load for 5 min, hold the load to collect the amount of fiber-optic grating wavelength, and by the test personnel to hold the crack viewer on the resulting crack measurements and records, the test force measurement system accuracy should not be greater than 1.0%, the resolution of the crack width measuring instrument should not be greater than 0.01 mm, loading should be avoided to avoid the eccentricity, to ensure that the concrete member of the compression end of the pressure uniformity of the force, the loading speed of not more than 100 MPa/min. The specimen installation schematic is shown in Figure 18. The specimen mounting diagram is shown in Figure 19.

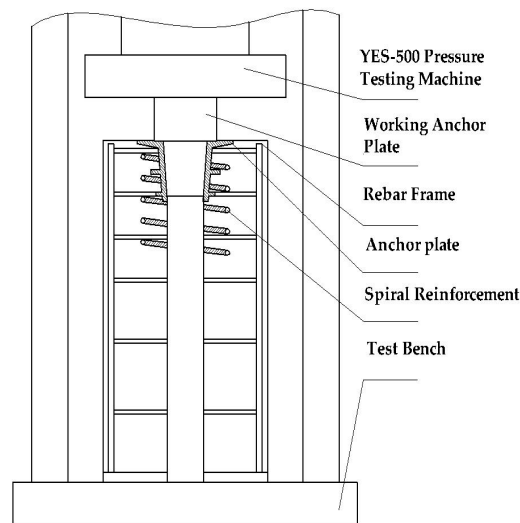


Figure 18. Specimen installation schematic.

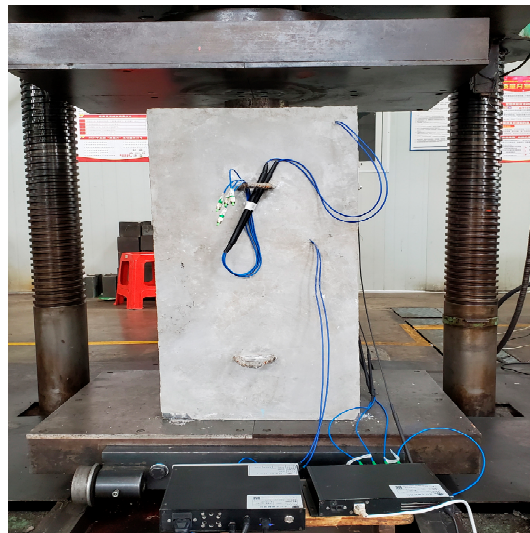


Figure 19. Specimen installation diagram.

The test pieces are made of C50 grade concrete and the specifications are $420 \times 420 \times 860$ mm, as shown in Table 6.

Table 6. Specimen specifications.

Name	Type Specification	Materials
Anchor plate	M15T-9D	HT200
Spiral reinforcement bellows	M15T-9/10L (C) Ø80 × 825	HPB300 -
Longitudinal reinforcement stirrup	Ø12 × 825 Ø16 × 374 × 374	HRB400 HRB400
Steel plate	420 × 420	Q235

Before the test, the FBG sensor is embedded in the screw bar to better monitor the change in screw bar strain with load. Bragg grating embedded spiral rib package steps: First, two grooves with a width of 1 mm and a depth of 1 mm are carved on the surface of the straight rib, and then the straight rib is bent into a spiral rib by coilers, and the FBG is pasted into the groove using epoxy resin. The pasting length is 40 mm, and the thickness of the pasting layer is 0.8 mm. This encapsulation method can avoid extrusion fractures

caused by direct contact between FBG and the matrix and improve the survival rate of FBG. The specific arrangement scheme of measuring points for the FBG spiral reinforcement strain sensor is shown in Figure 20. In the figure, L1 to L4 represent the positions of four measuring points. The spiral reinforcement used is HPB300 round steel with a diameter of 16 mm and a pitch of 55 mm, the diameter of the spiral reinforcement is 275 mm, and the number of turns is 5. The finished FBG spiral bar is shown in Figure 21.

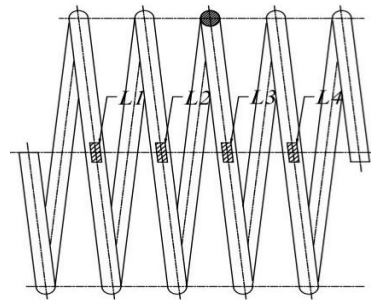


Figure 20. Schematic diagram of spiral bar measuring point layout.



Figure 21. Real picture of FBG spiral reinforcement.

The internal reinforcement size of the specimen is shown in Figure 22. Determine the size of the wooden mold according to the dimensions of the specimen structure, and the internal structure of the specimen is shown in Figure 23.

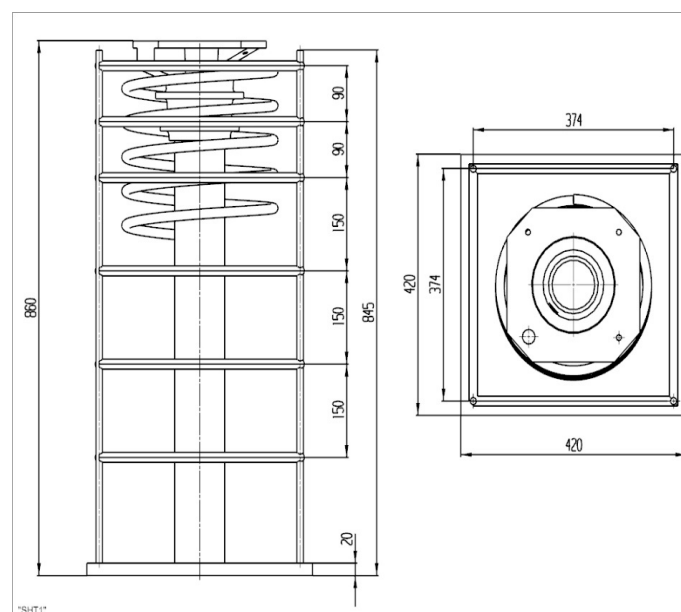


Figure 22. Schematic diagram of the internal reinforcement of the specimen.



Figure 23. Internal structure of test piece.

After the three concrete specimens are made, clean the dirt on the surface of the test pieces, sand the adhesive position of the fiber grating strain sensor on the surface of the concrete side to ensure the level of the side surface, mark the installation position of the base with a scratch needle, install the strain gauge base and fix it with hot melt adhesive, install the fiber grating strain sensor after the base is fixed, and arrange the transverse measurement points, as Figure 24 shows. The vertical measuring point arrangement is shown in Figure 25. The location of measuring points on the concrete surface is shown in Figure 26.



Figure 24. Layout of lateral measuring points.

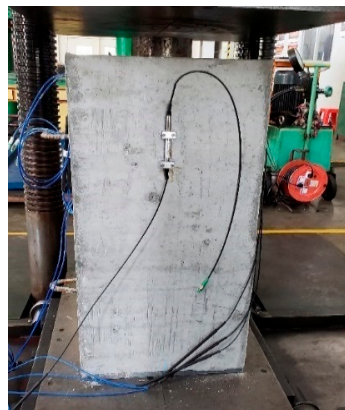


Figure 25. Layout of vertical measuring points.

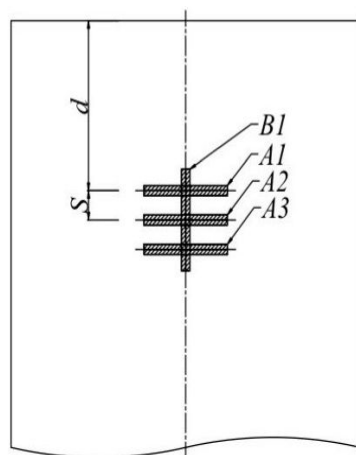


Figure 26. Schematic diagram of measuring points on the concrete surface.

5.2. Test Results and Analysis

The three cube concrete specimens No. 1, No. 2, and No. 3 used in this test were grouped, and each FBG spiral reinforcement sensor had 4 measuring points. The strain values of the FBG spiral reinforcement measuring points of the three specimens are shown in Table 7. The relationship between the strain and load grade of the three FBG spiral bars is shown in Figure 27.

Table 7. 1, 2, 3 samples FBG spiral bar measurement point response variables.

Load Class	Specimen No. 1				Specimen No. 2				Specimen No. 3			
	L1 / $\mu\epsilon$	L2 / $\mu\epsilon$	L3 / $\mu\epsilon$	L4 / $\mu\epsilon$	L1 / $\mu\epsilon$	L2 / $\mu\epsilon$	L3 / $\mu\epsilon$	L4 / $\mu\epsilon$	L1 / $\mu\epsilon$	L2 / $\mu\epsilon$	L3 / $\mu\epsilon$	L4 / $\mu\epsilon$
0.2 F_{ptk}	16.35	16.53	8.26	8.26	33.06	41.32	33.06	24.79	24.79	33.06	24.79	24.79
0.4 F_{ptk}	49.59	57.85	49.59	24.79	74.38	82.64	82.64	82.64	74.38	66.12	57.85	66.12
0.6 F_{ptk}	82.64	99.17	107.44	49.59	107.44	132.23	132.23	157.02	157.02	165.29	123.97	99.17
0.8 F_{ptk}	206.61	231.40	206.61	123.97	239.67	264.46	223.14	214.88	256.20	256.20	157.02	148.76
1.0 F_{ptk}	454.55	429.75	380.17	247.93	446.28	454.55	404.96	355.37	504.13	512.40	256.20	347.11
1.2 F_{ptk}	768.60	685.95	595.04	553.72	702.48	669.42	595.04	636.36	776.86	752.07	380.17	636.36

According to the results of FBG spiral reinforcement strain transducer measurements on specimens 1, 2, and 3, it can be seen that: with the gradual increase of load, the internal tensile strain of FBG spiral reinforcement of the three specimens gradually increased; in the range of 0~0.6 F_{ptk} , the internal tensile strain increases linearly; when the load reaches 0.8 F_{ptk} , the three specimens show the first crack, and then, due to the redistribution of stress between the concrete and spiral reinforcement, a steep increase in the internal strain occurs; in the range of 0.8~1.2 F_{ptk} , it continues to increase steeply. Therefore, there is a steep increase in the internal strain; the steep increase continues in the range of 0.8~1.2 F_{ptk} .

As can be seen from Table 8, the maximum tensile stresses of the measured FBG spiral reinforcement are all at the L2 position, which is the same as the position where the maximum main tensile stress of the spiral reinforcement appears in the finite element analysis. Before optimization of the anchor plate, the maximum tensile stress of the spiral reinforcement under the anchor ANSYS1 is greater than the measured average value by 10.51% to 39.18%. The maximum tensile stress ANSYS1 of the anchor plate with under-anchor spiral reinforcement before the optimization is greater than that of the anchor plate with under-anchor spiral reinforcement after optimization, ANSYS2, by 7.57~29.82%. After optimization of the anchor plate, the maximum tensile stress ANSYS2 of the spiral reinforcement under the anchor is consistent with the average value of the measured stress, which is larger by 2.74~8.51%.

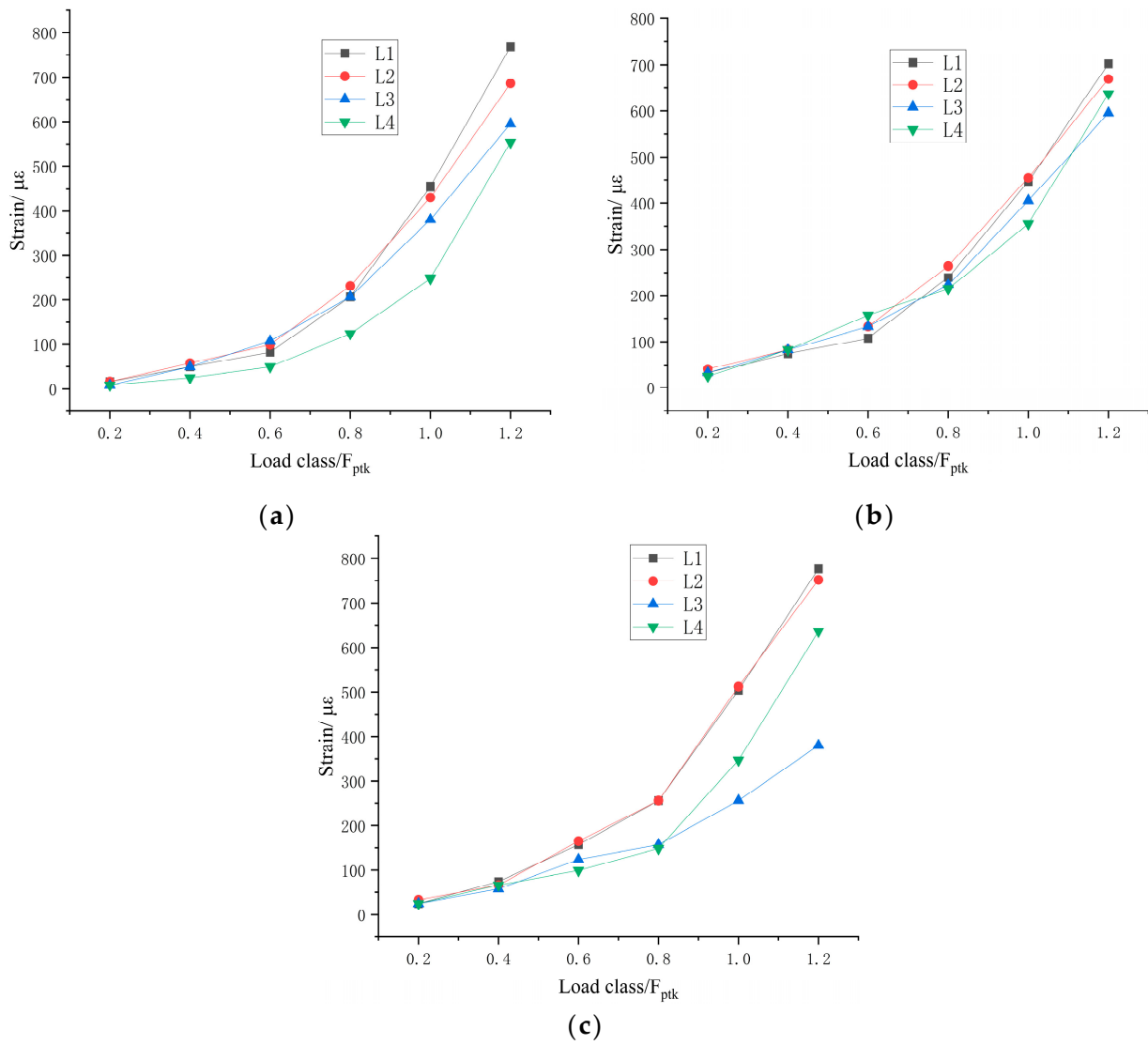


Figure 27. Strain-load grade relationship of three FBG spiral reinforcements: (a) Strain-load grade relation of specimen No. 1 FBG spiral reinforcement; (b) Strain-load grade relation of specimen No. 2 FBG spiral reinforcement; (c) Strain-load grade relation of specimen No. 3 FBG spiral reinforcement.

Table 8. 1, 2, 3 specimens FBG spiral bar stress value and finite element analysis comparison.

Load Class	Station Position	Specimen No. 1/MPa	Specimen No. 2/MPa	Specimen No. 3/MPa	Mean Value /MPa	ANSYS1 /MPa	ANSYS2 /MPa
0.2 F_{ptk}	L1	3.43	6.94	5.21	5.19	-	-
	L2	3.47	8.68	6.94	6.36	8.88	6.84
	L3	1.73	6.94	5.21	4.63	-	-
	L4	1.73	5.21	5.21	4.05	-	-
0.4 F_{ptk}	L1	10.41	15.62	15.62	13.88	-	-
	L2	12.14	17.35	13.89	14.46	17.77	15.69
	L3	10.41	17.35	12.15	13.30	-	-
	L4	5.21	17.35	13.89	12.15	-	-
0.6 F_{ptk}	L1	17.35	22.56	32.97	24.29	-	-
	L2	20.83	27.77	34.71	27.77	30.69	28.53
	L3	22.56	27.77	26.03	25.45	-	-
	L4	10.41	32.97	20.83	21.40	-	-

Finally, strain monitoring was carried out on the side surfaces of three cubic concrete specimens, and there were four FBG measuring points on each side surface. The strain values at each measuring point of FBG on the side surfaces of the three specimens are shown in Table 9. The relationship between the side surface tension strain and load grade of the three specimens is shown in Figure 28.

Table 9. Strain values of FBG concrete side surface measuring points of specimens 1, 2, and 3.

Load Class	Specimen No. 1				Specimen No. 2				Specimen No. 3			
	B1 / $\mu\epsilon$	A1 / $\mu\epsilon$	A2 / $\mu\epsilon$	A3 / $\mu\epsilon$	B1 / $\mu\epsilon$	A1 / $\mu\epsilon$	A2 / $\mu\epsilon$	A3 / $\mu\epsilon$	B1 / $\mu\epsilon$	A1 / $\mu\epsilon$	A2 / $\mu\epsilon$	A3 / $\mu\epsilon$
0.2 F_{ptk}	-36.49	17.27	7.93	3.7	-34.89	14.62	8.42	3.57	-30.03	11.60	7.62	3.67
0.4 F_{ptk}	-76.16	38.43	19.38	12.26	-74.10	42.98	24.51	11.11	-71.72	41.71	22.87	12.30
0.6 F_{ptk}	-123.22	59.42	39.85	29.30	-124.79	65.33	61.84	28.17	-131.04	59.86	38.57	27.92
0.8 F_{ptk}	-165.69	226.06	58.33	37.51	-171.90	534.58	183.28	54.15	-152.25	189.76	56.47	41.23

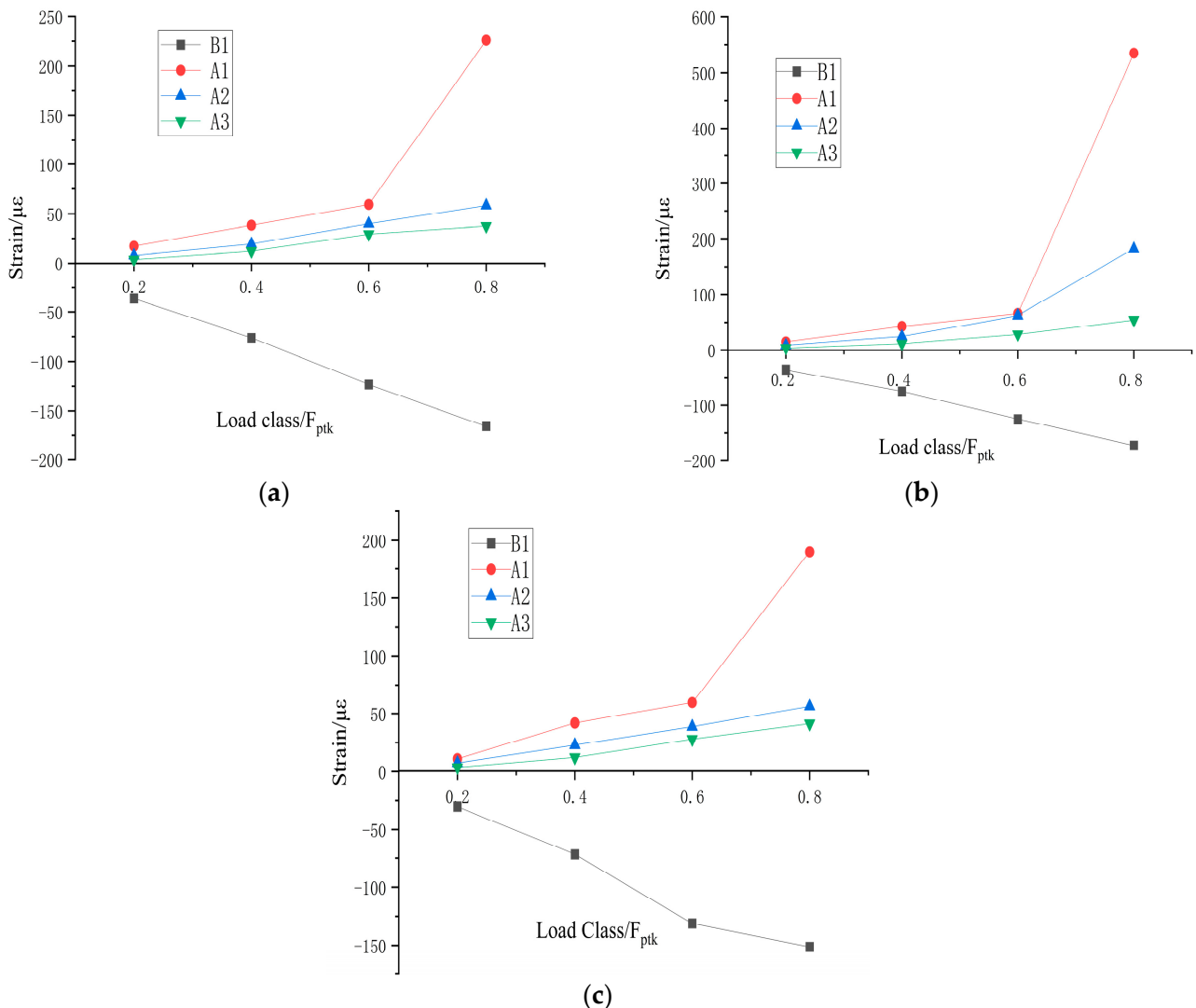


Figure 28. Strain-load grade relation of the concrete side surface of three specimens: (a) The lateral surface strain-load grade relation of specimen No. 1; (b) The lateral surface strain-load grade relation of specimen No. 2. (c) The lateral surface strain-load grade relation of specimen No. 3.

According to the results of the FBG concrete side surface strain transducer measurements of specimens 1, 2, and 3, it can be seen that the concrete surface tensile and

compressive strains gradually increase with the increase in load. In the range of $0\sim 0.6 F_{ptk}$, the concrete surface strain increases linearly. When the load reaches $0.8 F_{ptk}$, the three concrete specimens are in the first vertical splitting cracks; at this time, the concrete has exceeded the limit of its tensile strength, and the spiral reinforcement assists the concrete in absorbing the residual stress beyond the limit of its tensile strength, so the concrete specimen side of the surface of the lateral strain measured by the measuring point of the phenomenon of a steep increase.

As shown in Table 10, after finite element analysis, the value of concrete side surface stress in the anchorage zone of the optimized anchor plate with ANSYS2 is smaller than that of the pre-optimized anchor plate with ANSYS1, and the compressive stress has been reduced by 1.24~1.85% and the tensile stress has been reduced by 18.72~32.35%. The pre-optimized anchor plate has a larger value of concrete side surface stress ANSYS1 in the anchorage zone than the average value of measured side surface stress, with tensile stress being 10.85~36% larger and compressive stress being 11.24~39.66% larger. The optimized anchor plate has finite element analysis values of tensile stress on the concrete side surface of the anchorage zone ANSYS2, which are smaller than the measured average values by 8~9.91%.

Table 10. 1, 2, 3 specimens side surface stress values and finite element analysis comparison.

Load Class	Station Position	Specimen No. 1/MPa	Specimen No. 2/MPa	Specimen No. 3/MPa	Mean Value/MPa	ANSYS1 /MPa	ANSYS2 /MPa
0.2 F_{ptk}	B1	1.26	1.20	1.03	1.16	1.62	1.59
	A1	0.59	0.50	0.40	0.50	0.68	0.46
	A2	0.27	0.29	0.26	0.27	-	-
	A3	0.13	0.12	0.13	0.13	-	-
0.4 F_{ptk}	B1	2.63	2.56	2.47	2.55	3.23	3.19
	A1	1.32	1.48	1.44	1.41	1.57	1.27
	A2	0.67	0.85	0.79	0.77	-	-
	A3	0.42	0.38	0.42	0.41	-	-
0.6 F_{ptk}	B1	4.25	4.31	4.52	4.36	4.85	4.78
	A1	2.05	2.25	2.07	2.12	2.35	1.91
	A2	1.37	2.13	1.33	1.61	-	-
	A3	1.01	0.97	0.96	0.98	-	-

During the test, the hand-held portable measuring microscope was used to observe the crack width of the concrete side surface. The load ratings and specimen crack widths are shown in Table 11.

Table 11. Load rating and specimen crack width.

Load Class	Specimen Number	Crack Width/mm
0.8 F_{ptk}	Specimen No. 1	$\omega_1 = 0.07$
	Specimen No. 2	$\omega_1 = 0.08$
	Specimen No. 3	$\omega_1 = 0.06$
1.0 F_{ptk}	Specimen No. 1	$\omega_1 = 0.10; \omega_2 = 0.08; \omega_3 = 0.06$
	Specimen No. 2	$\omega_1 = 0.11; \omega_2 = 0.07$
	Specimen No. 3	$\omega_1 = 0.09; \omega_2 = 0.06; \omega_3 = 0.05$
1.2 F_{ptk}	Specimen No. 1	$\omega_1 = 0.12; \omega_2 = 0.09; \omega_3 = 0.08; \omega_4 = 0.05; \omega_5 = 0.04$
	Specimen No. 2	$\omega_1 = 0.15; \omega_2 = 0.09; \omega_3 = 0.05; \omega_4 = 0.05; \omega_5 = 0.04$
	Specimen No. 3	$\omega_1 = 0.10; \omega_2 = 0.08; \omega_3 = 0.06; \omega_4 = 0.04$

After observation:

- (1) When loading to $0.8 F_{ptk}$, the first crack appeared in the three concrete specimens, and the maximum crack widths were 0.07, 0.08, and 0.06 mm, respectively, which were all

less than the limit of 0.1 mm in FIP [28–30]. No other failure forms were found in the anchor plates of the three specimens.

- (2) When loading to $1.0 F_{ptk}$, the crack widths of the three concrete specimens continue to spread along the previous cracks, and new cracks are generated. The maximum crack widths do not exceed 0.11 mm. No other failure forms were found in the anchor plates of the three specimens.
- (3) When loading to $1.2 F_{ptk}$, the crack widths of the three concrete specimens continue to spread along the previous cracks, and new cracks are generated. The maximum crack widths do not exceed 0.15 mm. During the test, there is a slight subsidence around the anchor plate, the edge is slightly warped, and the whole structure of the anchor plate is not deformed.

6. Conclusions

Based on the theory of the strut-and-tie model, this paper optimizes the internal structure of the anchor plate based on the existing anchor plate and pours three concrete specimens for the anchorage zone force transmission test to verify the safety and reliability of the anchor zone at a 2200 MPa level using the optimized anchor plate:

- (1) After the three-dimensional model establishment, finite element analysis, and establishment of the strut-and-tie model, in the second pressure-bearing step anchor plate, based on the addition of the middle third pressure-bearing step, the angle of its anchorage zone strut-and-tie model increased. The anchor plate increases, the middle pressure-bearing step position is different, and its anchorage zone strut-and-tie model strut and compression rod angle are different. Optimizing the design of the anchor plate according to the 0.533 position parameter of the intermediate pressure-bearing step, the angle of the strut-and-tie model in the anchorage zone is the largest, and the bearing capacity of the anchorage zone is relatively high. The change in the internal structure of the anchor plate affects the stress distribution in the anchorage zone.
- (2) Comparative analysis by finite element. According to the middle pressure-bearing step position parameter of 0.533 to optimize the design of the anchor plate, the main tensile and compressive stresses of the anchor plate after optimization increased by 6.2% and 5.74%, respectively, compared with the anchor plate after optimization. The main tensile stress of the spiral reinforcement under the anchor decreased by 0.59%, the main compressive stress increased by 2.89%, and the Von Mises tensile stress decreased by 2.32%. The side surface tensile stress of concrete under the anchor decreased by 4.3%.
- (2) After the anchorage zone force transfer test, through the use of FBG strain transducer measured 1, 2, and 3 specimens are in the load $0\sim 0.6 F_{ptk}$, the spiral reinforcement strain value, the concrete side surface strain value show a linear growth, the finite element simulation stress value and the average value of the measured stress comparison of the basic match, the spiral reinforcement finite element stress simulation value compared with the average value of the measured stress is greater than the average value of the stress by 2.74~8.51%, the spiral reinforcement finite element stress simulation value compared with the average value of the measured stress is greater by 8~9.91%. The concrete side surface finite element analysis stress value is smaller than the average value of measured stress by 8~9.91%. Under the load of $0.8 F_{ptk}$, the first crack appeared in all three concrete specimens, due to the stress redistribution, the strain of spiral reinforcement, and the concrete side surface strain are steeply increasing phenomena, and the width of the crack is not more than 0.08 mm. When the load is loaded to $1.2 F_{ptk}$, the maximum value of the specimen's crack width is not more than 0.15 mm, which meets the requirements of the FIP's crack width limit, and the anchor plate has no deformation except the slight subsidence around the anchor plate. There was no overall deformation except for a slight subsidence around it. Therefore, it is further verified that the anchor plate after optimization designed according to the intermediate pressure-bearing step position parameter 0.533 is structurally safe

and suitable for a 2200 MPa grade high-strength strand, and its 2200 MPa grade prestressing anchorage zone has sufficient bearing capacity.

Author Contributions: Conceptualization, W.Z.; methodology, W.Z.; software, X.L.; validation, W.Z. and X.L.; tests, data interpretation, and writing—original draft preparation, X.L.; writing—review and editing W.Z. and X.L. Data interpretation and writing—original draft preparation X.L. All authors have read and agreed to the published version of the manuscript.

Funding: This study was funded by the National Natural Science Foundation of China (Grant No. 52068014), Guang Xi Innovation-driven Development project (Grant No. AA20302006), Hunan Provincial Department of Transportation Science and Technology Plan Project (Grant No. 202015).

Data Availability Statement: The original contributions presented in the study are included in the article, further inquiries can be directed to the corresponding author.

Acknowledgments: The authors would like to express their gratitude for the support of the Nation Science Foundation of China, the Guang Xi Innovation-driven Development project and Hunan Provincial Department of Transportation Science and Technology Plan Project.

Conflicts of Interest: The authors declared that they have no conflicts of interest in this work.

References

1. Rebelo, J.; Marchão, C.; Lúcio, V. Study on the efficiency of confinement reinforcement in post-tensioning anchorage zones. *Mag. Concr. Res.* **2019**, *73*, 1–39.
2. Shin, J.; Kim, J.H.; Chang, H.J. Anchor plate effect on the breakout capacity in tension for thin-walled concrete panels. *Eng. Struct.* **2016**, *106*, 147–153. [[CrossRef](#)]
3. Kwon, Y.; Kim, J.K.; Yang, J.M. Development of Efficient Anchorage Device and Estimation of Its Bearing Strength of Posttensioning Anchorage Zone. *J. Struct. Eng.* **2017**, *144*, 04017219. [[CrossRef](#)]
4. Ji, J.H.; Dong, Z.Q.; Liu, Z.Q.; Sun, Y.; Zhu, H.; Wu, G. Chee-Kiong Soh, Feasibility of using Fe-SMA rebar as cracking resistance spiral stirrup in the anchorage zone of post-tensioned prestressed concrete. *Structures* **2023**, *48*, 823–838. [[CrossRef](#)]
5. Vladimir, C.; Rudolf, G.H. Validation of post-tensioning anchorage zones by laboratory testing and numerical simulation. *Struct. Concr.* **2014**, *15*, 258–268.
6. Mao, W.Z.; Gou, H.Y.; He, Y.N.; Pu, Q.H. Local Stress Behavior of Post-Tensioned Prestressed Anchorage Zones in Continuous Rigid Frame Arch Railway Bridge. *Appl. Sci.* **2018**, *8*, 1833. [[CrossRef](#)]
7. Kook, K.J.; Yangsu, K.; Gyoung, K.H. Anchorage Zone Behavior in the Slab with Flat Anchorage. *J. Korean Soc. Hazard Mitig.* **2014**, *14*, 1738–2424.
8. Chen, D.S.; Cao, G.K. Finite element analysis of high strength environmental prestressed anchor anchor plate. *Sichuan Build. Mater.* **2019**, *45*, 162–163. (In Chinese)
9. Shi, L.; Ma, L.; Chen, S.L.; Su, Y.H. Research on High-strength Prestressed Anchorage System Technology of Railway Bridge. *Railw. Eng.* **2021**, *61*, 1–4+39. (In Chinese)
10. Ma, Q.; Zhu, W.X.; Su, H.T.; Fu, W.; Yang, B.D. Optimization Design for Prestressed Anchor plate Structure. *J. Sichuan Univ. Sci. Eng. (Nat. Sci. Ed.)* **2014**, *27*, 8187. (In Chinese)
11. Zhao, Y.; Li, D.B.; Cheng, Z.J.; Zhu, W.X.; Zhou, J.M. Experimental study of the load transfer behavior of post-tensioned concrete anchorage zone with cast anchor plate. *China Civ. Eng. J.* **2011**, *44*, 47–54. (In Chinese)
12. Chen, J.Y.; Xie, X.; Xu, A.M. Study of tendon anchorage zones of long span post tensioned prestressed concrete box girder. *J. Zhejiang Univ. (Eng. Sci.)* **2009**, *43*, 1077–1082, 1176.
13. Zhu, W.X.; Qin, H.Y.; Gan, G.R.; Fu, W. Key Techniques of Prestressed High-strength Rebar Anchorage Structure for Segmental Precast Piers of Hong Kong-Zhuhai-Macao Bridge. *J. China Railw. Soc.* **2017**, *39*, 118–124. (In Chinese)
14. Zhu, W.X.; Zhang, H.L.; Gan, G.R.; Fu, W. Experimental Research on Prestressed High Strength Rebar Anchorage System for Segmental Precast Piers of Hong Kong-Zhuhai-Macao Bridge. *Constr. Technol.* **2017**, *46*, 101–105. (In Chinese)
15. Aashto, L.R.F.D. *Bridge Design Specifications*, 9th ed.; American Association of State Highway and Transportation Officials: Washington, DC, USA, 2020.
16. Zhou, L.Y.; Wan, S. Full-range nonlinear analysis of post-tensioned anchorage zones based on modified strut-and-tie model. *Structures* **2022**, *35*, 565–576. [[CrossRef](#)]
17. Cui, N.N.; Huang, S.P. On the optimal strut-and-tie models and design approach for the cable-pylon anchorage zone. *J. Civ. Eng. Manag.* **2019**, *25*, 576–586. [[CrossRef](#)]
18. Hou, D.W.; Zhao, J.L.; Shen, S.L.; Chen, J. Investigation and improvement of strut-and-tie model for design of end anchorage zone in post-tensioned concrete structure. *Constr. Build. Mater.* **2017**, *136*, 482–494. [[CrossRef](#)]
19. Lin, B.; Liu, Z. Strut-and-tie model and reinforcement design method for isolated rectangular anchor block for external tendons. *Eng. Mech.* **2011**, *28*, 59–64. (In Chinese)

20. Zaborac, J.; Choi, J.; Bayrak, O. Assessment of deep beams with inadequate web reinforcement using strut-and-tie models. *Eng. Struct.* **2020**, *218*, 141–296. [[CrossRef](#)]
21. Kumar, A.; Jangid, R.S. Strength prediction of a bottle-shaped strut for evaluating the shear capacity of reinforced concrete deep beam. *Eng. Res. Express* **2023**, *5*, 015048. [[CrossRef](#)]
22. Hamid, K.; Abolfazl, A. A STM-based analytical model for predicting load capacity of deep RC beams with openings. *Structures* **2021**, *34*, 1185–1200.
23. Panatchai, C.; Jaruek, T.; Sukit, Y. Modified interactive strut-and-tie modeling of reinforced concrete deep beams and corbels. *Structures* **2022**, *45*, 284–298.
24. Yi, W.J.; Li, Y.; Chen, H.; Ma, J.Z.G.; Zhou, K.J.; Huang, Y.; Zhou, Y. Shear strength evaluation of RC D-Regions based on Single-Panel Strut-and-Tie model. *Eng. Struct.* **2022**, *265*, 114500. [[CrossRef](#)]
25. Li, S.S.; Zheng, J.Y.; Zhang, F.J.; Li, H.M.; Jia, M.X.; Liu, Z.J.; Chen, A.J.; Xie, W. Prediction of Shear Strength for Steel-Fiber High-Strength Concrete Corbels with the Softened Strut-and-Tie Model. *Buildings* **2023**, *13*, 1107. [[CrossRef](#)]
26. Ministry of Housing and Urban-Rural Development. *TB/T3193-2016 PRC; Clamp Type Anchors, Clamps and Connectors for Prestressed Tendons in Railway Engineering*. China Building Industry Press: Beijing, China, 2016. (In Chinese)
27. Zhao, J.L.; Shen, S.L.; Sun, Y. Application of Strut-and-tie Model for Design of Interior Anchorage Zone in Post-tensioned Concrete Structure. *J. Shanghai Jiao Tong Univ. (Sci.)* **2010**, *15*, 273–278. (In Chinese) [[CrossRef](#)]
28. FIP Recommendations. *Acceptance of Post-Tensioning Systems*; International Federation of Structural Concrete FIB: Lausanne, Switzerland, 2010.
29. CEB-FIP. *CEB-FIP Model Code 1990: Design Code*; Thomas Telford Publishing: London, UK, 1993.
30. ACI (American Concrete Institute). *Building Code Requirements for Structural Concrete and Commentary*; American Concrete Institute: Farmington Hills, MI, USA, 2019; pp. 318–319.

Disclaimer/Publisher’s Note: The statements, opinions and data contained in all publications are solely those of the individual author(s) and contributor(s) and not of MDPI and/or the editor(s). MDPI and/or the editor(s) disclaim responsibility for any injury to people or property resulting from any ideas, methods, instructions or products referred to in the content.